Investigating Charge Transfer in Functionalized Mesoporous EISA-SnO 2 Films

Wael Hamd, Christel Laberty-Robert, François Lambert, Cyrille Costentin, Benoit Limoges, Veronique Balland

THE JOURNAL OF PHYSICAL CHEMISTRY C

Article

Investigating Charge Transfer in Functionalized Mesoporous EISA-SnO Films

Wael Hamd, Christel Laberty-Robert, François Lambert,
Cyrille Costentin, Benoit Limoges, and Veronique Balland

J. Phys. Chem. C, **Just Accepted Manuscript** • DOI: 10.1021/acs.jpcc.7b07071 • Publication Date (Web): 25 Sep 2017

Just Accepted

ACS Publications

The Journal of Physical Chemistry C is published by the American Chemical Society.
1155 Sixteenth Street N.W., Washington, DC 20036

Investigating Charge Transfer in Functionalized Mesoporous EISA-SnO_2 Films

Wael Hamd,[†] Christel Laberty-Robert,[#] François Lambert,[§] Cyrille Costentin,[†] Benoît Limoges[†,*] and Véronique Balland[†,*]

[†] *Laboratoire d'Electrochimie Moléculaire, UMR 7591 CNRS, Université Paris Diderot, Sorbonne Paris Cité, 15 rue Jean-Antoine de Baïf, F-75205 Paris Cedex 13, France*

[#] *Sorbonne Universités, UPMC Univ Paris 6, CNRS, Collège de France, Laboratoire de Chimie de la Matière Condensée de Paris, 4 place Jussieu, F-75005 Paris, France.*

[§] *Laboratoire des Biomolécules, UMR 7203 CNRS, UPMC Univ Paris 6, Ecole Normale Supérieure, 24 rue Lhomond, F-75005 Paris, France.*

ABSTRACT. Semiconductive transparent thin films of periodically-organized nanostructured SnO_2 were prepared on flat conductive ITO substrates by evaporation-induced self-assembly (EISA) under different dip-coating regimes and then functionalized by two redox-active chromophores, i.e. the flavin mononucleotide (FMN) able to reversibly exchange 2 e^- and 2 H^+ and the $[Os^{II}(bpy)_2(4,4'\text{-}CH_2PO_3H_2\text{-}bpy)]^{2+}$ complex (OsP) involving a fast and reversible one-electron transfer**.** The redox behavior of these two chemisorbed chromophores was investigated by cyclic voltammetry and cyclic voltabsorptometry. On account of the distinct formal potential of the two redox chromophores relative to the position of the lower conduction band edge of SnO_2, the heterogeneous electron transfer was observed either reversible (FMN) or irreversible (OsP). In the case of the OsP-functionalized SnO_2 electrode, quantitative analysis of the cyclic voltabsorptograms was achieved within the framework of our previously proposed kinetic model of charge transfer/transport in mesoporous semiconductive films (Renault *et al.*, *Phys. Chem. Chem. Phys.* **2015**, *17*, 10592–607), allowing for direct comparison between EISA-TiO_2 and EISA-SnO_2 electrodes. It is notably shown that the interfacial electron transfer between the adsorbed redox chromophore and the SnO_2 interface is the rate-determining process under our experimental conditions. It is additionally demonstrated that the electrons trapped in the low-energy surface states of EISA-SnO_2 can directly participate to the interfacial electron transfer, a behavior that strongly contrasts to that we had previously found at EISA-TiO_2 electrodes (i.e., wherein only electrons from the conduction band were involved in the interfacial electron transfer).

INTRODUCTION

Photoanodes based on nanoporous semiconductive films of SnO_2 are recognized as an alternative to the much more widely explored nanoporous films of TiO_2, especially as part of photoelectrocatalytic cells (DSPECs) operating under sunlight irradiation.[1,2] Essential to the development of such photoanodes is the sensitization of the porous transparent semi-conductive metal oxide film by redox-active chromophores that adsorb visible light and promote fast electron injection into the conduction band of the semiconductor. The ensuing photo-oxidized chromophore can then be used either directly or indirectly (i.e., through the intermediate of a co-immobilized catalyst) to oxidize a substrate in solution (e.g., water in the case of a water-splitting DSPEC). The main advantage of SnO_2 over TiO_2 is its conduction band potential shifted ~0.4 V more positive than TiO_2,[3,4] expanding thus the choice of redox-active chromophores that feature less reducing excited states and in turn higher ground-state oxidation potentials (which is beneficial to drive the oxidation of water in a water-splitting DSPEC or any other molecules difficult to oxidize in others photoelectrocatalytic applications).[5–8] Others advantages of SnO_2 rely on its wide band gap (~3.6 eV), therefore decreasing complications from direct band gap excitation and promoting long term stability under the harsh chemical conditions generally involved in DSPEC applications. This is also a n-type semiconductor that leads to faster electron transport characteristics than TiO_2.[9] Such faster electron transport should theoretically favor the collection efficiency of photoinjected electrons at the expense of losses by interfacial charge transfer recombination. However, despite this, only poor device efficiencies have been reported to date with nanoporous SnO_2-based photoanodes.[2]

Better understanding the factors limiting the performance of nanoporous SnO_2 photoanodes compared to those based on other nanostructured metal oxides is therefore key to better assess

the actual potentialities offered by this material in DSPEC applications. These factors include not only the dynamics of electron transport by diffusion throughout the mesoporous metal-oxide network, but also the interfacial electron transfer kinetics associated both to the photoinjection of electrons in SnO_2 and to the back electron transfer (BET) resulting from charge recombination between electrons injected in SnO_2 and the oxidized dye or species present in solution. Several studies have already addressed the electron injection dynamics in SnO_2 from diverse photoexcited redox dyes adsorbed in nanocrystalline films.[4,9–13] Electron injection rates were shown to proceed within the pico- to nanosecond range, which is ~1 order of magnitude lower than for TiO_2. This lower injection rate has been attributed to a lower density of states in the conduction band of SnO_2 compared to TiO_2 (the available density of states is almost two orders of magnitude higher in TiO_2 than in SnO_2).[14] Interfacial charge recombination in dye-sensitized nanoporous SnO_2 films have also been the subject of several studies.[4,15,16] These BET reactions are undesired since they compete with the substrate oxidation in solution, contributing thus to the loss of DSPEC performance. Consequently, minimizing the interfacial charge recombination is key for developing efficient DSPEC devices. BET rates in dye-sensitized SnO_2 or TiO_2 films were found to occur within the micro- to millisecond time scale, depending on the nature of the excited dye and electrolyte solution. BET rates were found significantly higher in SnO_2 than in TiO_2 (roughly 2 orders of magnitude faster in SnO_2 than TiO_2 when working in organic media and only 2-3 fold faster when operating in an aqueous acidic electrolyte), a behavior that was attributed to differences in the energy distribution and density of intra-band-gap states (i.e., including bulk trap states and surface states). [4,15,16] Faster electron diffusion in SnO_2 was indeed attributed to a lower bulk trap density,[4] while the role of surface states in the recombination process was evidenced from atomic layer deposition of conformal thin passivating coatings of

Al_2O_3 or TiO_2 on the surface of mesoporous SnO_2 films, resulting thus in a decrease of the recombination rates.[17,18]

In an attempt to better understand the key factors governing the BET reactions in semiconductive nanostructured SnO_2 films, we investigate here by real-time cyclic voltabsorptometry the redox behavior of two different redox-active chromophores that are strongly chemisorbed on the surface of highly-ordered mesoporous thin films of SnO_2. The methodology used for extracting the key information is similar to the one we have recently developed for analyzing the interfacial electron transfer parameters in mesoporous films of TiO_2 functionalized by iron-porphyrin-based compounds.[19] The SnO_2 films are prepared by evaporation-induced self-assembly (EISA), a sol-gel surfactant-templated synthetic method which leads to the formation of highly periodically-organized nanoporous metal oxides thin films on a flat solid substrate (i.e. a transparent conductive ITO electrode in the present case).[20] The main interests of these mesoscopic films are their well-defined porosity, well-controlled 3D organization, high specific surface area, and relatively robust inorganic structure made of thick semicrystalline walls. These specific properties are not only advantageous for the development of efficient DSPEC devices but also useful for fundamental studies whose objective is to quantitatively analyze the different modes of charge transfer/transport in these highly-organized films. Still, only a few papers report on the preparation of crystalline mesoporous SnO_2 films by EISA.[21] This can be explained by the difficulties encountered during the crystallization process at high temperature, difficulties that however can be overwhelmed with amphiphilic block-copolymers organic templates ("KLE" type) on account of their better thermal stabilities than pluronic templates.[21] In the present study, we demonstrate that highly nanoporous crystalline EISA-SnO_2 thin films can be obtained from commercial block copolymers of polyisobutylene-

polyethylene oxide (PIB–*b*–PEO). Additionally, the film thickness (~250 nm) is shown to be maximized by adjusting the one-step dip-coating process at very low withdrawal speeds (i.e., draining regime).[22] The resulting SnO_2 films are chemically functionalized by Flavin mononucleotide (FMN, able to reversibly exchange 2 e- and 2 H^+) or the $[Os^{II}(bpy)_2(4,4'\text{-}CH_2PO_3H_2\text{-}bpy)]^{2+}$ complex (OsP, a one-electron transfer complex) through chemisorption of their phosphate/phosphonate anchoring group and characterized by cyclic voltabsorptommetry. On account of the distinct formal potential of the two redox chromophores relative to the position of the lower conduction band edge of SnO_2, the heterogeneous electron transfer is shown either reversible or irreversible. In the case of the irreversible charge transfer with the OsP-functionalized EISA-SnO_2 electrode, it is found that electrons trapped in the low-energy surface states of EISA-SnO_2 can directly participate to the interfacial electron transfer. This observation contrasts to our previous results with mesoporous EISA-TiO_2 films wherein the interfacial electron transfer to an absorbed redox compound was shown to proceed exclusively through the extended conduction band states.[19] The present results confirm that multiple interfacial recombination pathways coexist in mesoporous SnO_2 electrodes and that the localized low-energy surface states contribute significantly to the undesirable charge recombination, a process that has been previously suggested to predominate in mesoscopic SnO_2 films than TiO_2 films.[17,18]

EXPERIMENTAL DETAILS

Chemicals. Tin tetrachloride (99%), and solvents were purchased from Sigma Aldrich, polyisobutylene-polyethyleneoxide (PIB-b-PEO; reference P4973-ibEO: MWPIB= 7000 g·mol^{-1}, MWPEO ¼ 8500 g·mol^{-1}) was purchased from Polymer Source. All the chemical reagents used in the experiments were obtained from commercial sources as guaranteed-grade reagents and used without further purification. The osmium complex $[Os(bpy)_2(4,4'\text{-}(CH_2PO_3H_2)bpy)]Cl_2$ (OsP) was prepared according to a procedure described for Ruthenium.[23] The product was characterized by cyclic voltammetry in a Hepes Buffer solution (pH 7) by a single reversible wave centered at 0.6 V vs Ag/AgCl. Planar ITO-glass substrates were purchased from SOLEMS.

Synthesis of templated SnO_2. 175 mg of PIB-b-PEO was dissolved in a mixture of 5.6 g EtOH and 0.4 g H_2O by careful heating to 70 °C for 1 hour. After cooling for several minutes, 1.2 g of $SnCl_4$ was added dropwise. Then, the solution was stirred for 48 h. The resulting clear solution was dip-coated at ambient temperature on commercial ITO-coated glass substrates to produce thin films.

All films were prepared using a new generation homemade dip-coater (from SolGelWay). Films were deposited at a relatively low humidity (20%) at withdrawal speeds ranging from 0.01 to 5 mm s^{-1} and at room temperature. The whole dip-coater was isolated from natural vibration and external convection so as to prevent the formation of horizontal strips (thickness non-uniformity) associated with the fluctuation of the solution surface that creates meniscus instability. In the present investigation, the same container was used to make sure the meniscus shape was similar for each experiment and also to diminish the potential fluctuation of the meniscus height during deposition due to vibration-induced surface instability. These controls are necessary for ultralow withdrawal speeds. After complete drying in air, hybrid films were

directly transferred underneath a curing IR lamp to be thermally treated at 500 °C in air for 1 hour to decompose the organic parts, to complete the inorganic condensation and to induce the crystallization of SnO_2.

Ellipsometry. The thickness (*h*) and the refractive index (*n*) of optical films were measured by ellipsometry under UV-visible light at 70° variable angles. Thermal ellipsometry analysis was performed between 80 and 500 °C to determine the most adequate heat-treatment for the transformation of the hybrid organic inorganic film into a crystalline mesoporous films Measurements were performed in the wavelength range of 400 to 900 nm, using a covered heating unit connected and monitored by a programmable temperature regulator. The thermocouple regulator was directly in contact with the sample.

After dip-coating, the as-prepared hybrid organic–inorganic films deposited onto silicon wafer were heated at 80 °C for 10 minutes inside the covered heating unit, just before analysis measurements. Data analysis was performed with Wvase32 software, where ellipsometric data tan(C) and cos(D) were fitted using a single Lorentz oscillator layer model with one oscillator with center energy fixed at zero and other with free center energy in the UV-visible domain. The thickness (*h*), the real (*n*) and imaginary (*k*) parts of the complex refractive index of the films were also evaluated.

Environmental ellipsometry porosimetry (EEP). Investigations were conducted at room temperature (25°C) using the adsorption–desorption isotherm of water analyzed with an isotropic inorganic pore contraction model (IIC) and a modified Kelvin equation for ellipsoidal pores. Pore volume and adsorbed water content were estimated through the Bruggeman Effective Medium Approximation using the optical properties of the pure media (ZnO, SiO_2, air and H_2O). The ellipsometer was fitted with a small, variable humidity flow chamber (SOPRA) flushed with 2.5

L of air per min. The humidity was adjusted using a mass flow controller and monitored using a relative humidity probe held in the environmental chamber.

SEM FEG, EDX. The microstructures of the films obtained at different withdraw speed were observed by Field Emission (FE) Gun Scanning Electron Microscopy (FE-SEM, Hitachi). The chemical compositional analysis of the films was performed by Energy Dispersive X–ray spectroscopy.

XRD. The structure of the mesoporous SnO_2 films was determined using a prototype X-ray diffractometer equipped with a curved position sensitive detector (120°) from Inel. A fixed-incidence monochromatic CoKα impinging parallel beam is obtained by refection on a flat Ge(111) crystal. Cobalt radiation was used instead of more usual copper radiation to avoid sample fluorescence. The beam cross-section was 0.05×6 mm^2, producing a rectangular 3x6 mm^2 beam footprint on the sample at a fixed incidence of 1°. At this incidence, the attenuation length inside the hematite sample is about 0.7 mm. The grazing incidence diffraction patterns ($0 < 2\theta < 120°$, $\Delta 2\theta = 0.015°$, $\alpha=1°$) were refined using the Rietveld software XND. The broadening components related to finite crystallite size and microstrain were determined after taking into account the specific corrections for the instrumental broadening related to the grazing incidence setup.

Electrode Functionalization. Adsorption of the water-soluble redox probes (FMN or OsP) into the highly ordered mesoporous structure of SnO_2 thin films (~250-nm thick) was achieved at room temperature by immersing the mesoporous SnO_2-coated ITO glass plates in a 1 mM milli-Q aqueous solution (pH ~5) of each redox probe for few hours (> 2 hours). After adsorption, the modified electrodes were carefully rinsed with milli-Q water and soaked for 1 hour in the buffer

solution (50 mM Hepes, 300 mM KCl, pH 7.0) to desorb low affinity fractions of the redox probes prior characterization by spectroelectrochemistry.

Spectroelectrochemistry. For spectroelectrochemical experiments, a TORUS UV-visible diode-array spectrophotometer (Ocean Optics), equipped with optical fibers and a balanced deuterium tungsten source (Micropack), was coupled to an Autolab potentiostat PGSTAT 12 (EcoChemie) interfaced to a PC computer (GPES software). Both instruments were synchronized through an input trigger signal generated from the potentiostat, allowing thus to simultaneously recorded the change of optical absorbance during a chronoamperometric or a cyclic voltammetric scan. The spectroelectrochemical measurements were performed in a home-made one-compartment three-electrode cell. The SnO_2-film-coated ITO glass substrate was used as the working electrode, whereas a platinum wire and Ag/AgCl electrode in 3 M KCl were used as counter and reference electrodes, respectively (i.e., +0.20 V vs. NHE at 20°C). All potentials in the work were quoted to this reference electrode. The working electrode was prepared from a small rectangular piece of 0.8 × 3.5 cm cut from a SnO_2-film-coated ITO glass plate. A working area of 0.30 ± 0.05 cm^2 was delimited from one extremity of the rectangular piece by depositing an insulating layer of varnish.

The three electrodes were inserted in a 1-cm path length quartz cell through a silicon cap that hermetically closes the cell. An additional Tygon tube was introduced for degassing. The spectroelectrochemical cell was filled with 1.5 mL buffer and was thoroughly freed of air by bubbling with argon prior to the experiments. During the experiments, argon was continuously flowed over the solution in order to maintain the anaerobic environment and the cell was thermostated to 20°C using a Peltier-controlled cuvette holder (Quantum Northwest). All

experiments were carried out in an aqueous buffer of 50 mM Hepes (pH 7 and pH 8.5) or 50 mM MES (pH 5 and pH 6), in the presence of 300 mM KCl.

RESULTS AND DISCUSSION

Preparation of the EISA-SnO_2 thin films.

The mesoporous SnO_2 films were synthesized onto a flat conductive ITO-coated glass substrate by a template-directed sol–gel synthesis coupled with a one-step dip–coating process. Different withdrawal speeds were used for the dip–coating deposition allowing different deposition regimes, i.e. the draining regime at high-speed values (> 1 $mm{\cdot}s^{-1}$) and the capillary regime at speeds below 0.1 $mm{\cdot}s^{-1}$. The later allows for SnO_2 films characterized by a larger thickness and thus a higher specific surface area enhancement.[22]

For all deposition regimes, dip-coating of the precursor sol resulted in an initial hybrid transparent and homogeneous amorphous film, as indicated by the X-ray diffraction patterns. High temperature annealing of the hybrid organic–inorganic films is then required to obtain a crystalline material with an open porosity network. We have investigated the thermal behavior of the hybrid organic–inorganic SnO_2 films in the draining regime by thermoellipsometry in order to propose the adequate heat-treatment that (i) keeps the organization of pores defined by the organic template in the hybrid organic–inorganic films and (ii) allows for a good crystallization of the inorganic walls. The variation of SnO_2 film thickness as a function of temperature is reported in Figure S1. The derivative curve exhibits three main peaks related to various phenomena. The first peak at low temperature (~120°C) corresponds to a thickness decrease resulting from the evaporation of residual solvents such as H_2O and EtOH. Between 220 °C and

250 °C, variations of both thickness and refractive index are observed. It corresponds to the decomposition of PEO and PIB blocks to CO and CO_2 gases. Between 400 °C and 450 °C, the low decrease of the thickness with temperature can be attributed to the crystallization of SnO_2 nanocrystallites (by a nucleation and growth process). XRD peaks are characteristic of cassiterite, a crystalline morphology identified on the X-ray diffraction patterns of 500 °C calcined films. The decomposition of the different blocks thus occurs prior to the crystallization of SnO_2 at around 450 °C. But, the final refractive index following this heat treatment is quite high compared to those obtained by flash treatment at 500 °C, indicating the formation of the porous network. Note that flash annealing induces an important inorganic growth leading to the collapse of the pore structure. Accordingly, a thermal treatment at 500 °C in air for 1 hour was required to form a nanostructured, mesoporous film of SnO_2 with a well-defined and highly accessible porous network, allowing fast diffusion of chemicals.

Physical characterization of the EISA-SnO_2 thin films.

The thickness of single-dip-coated mesoporous films, heat-treated at 500 °C, has been evaluated by FE-SEM analyses and the value is comparable to that estimated by ellipsometry, within the experimental errors (Table 1). Top-down and cross-section images show highly porous and uniform heat-treated films (Figure 1). As expected, a much higher film thickness of ca. 250 nm could be obtained in the capillary regime (withdrawal speed of 0.01 $mm \cdot s^{-1}$) than in the draining regime wherein the maximum film thickness reached was only 100 nm (at a withdrawal speed of 5 $mm \cdot s^{-1}$). For the larger film, the cross-section image shows ellipsoidal pores which is attributed to a small contraction of the film during calcination / crystallization.

The composition of the nanostructured SnO_2 films was determined by EDX analyses (Figure S2). We found that the principal element (Sn) was homogeneously distributed within the film.

We also denote the existence of (In) and (Si,Na) elements from the underlying ITO-glass substrate.

The porosity of the EISA-SnO_2 films was analyzed by ellipsometric porosimetry. A similar behavior was observed for the 100- and 250-nm thick SnO_2 films prepared at 5 and 0.01 $mm \cdot s^{-1}$, respectively. The water adsorption/desorption isotherm is shown in Figure S3, and the corresponding pore size distribution plots calculated from both adsorption and desorption branches are given in Figure 1. Firstly, as expected from the very low refractive index (n = 1.22), the accessible porosity is very high since one found 65-70% in total volume. This value was obtained based on the Brugeman Effective Medium Approximation (BEMA), using n = 2 at 700 nm for the theoretical refractive index for crystalline bulk SnO_2. The adsorption and desorption curves are almost overlapping over the humidity range, which suggests that the porosity is highly accessible, as one would expect from a 3D fully interconnected void network. Such an hysteresis suggests absence of restrictions, or presence of wide ones, which would then imply that pores are close to interconnected channels or open tubes.[24,25] Assuming so, and using the 27° (measured value) as the water contact angle on SnO_2 surface model in the Kelvin equation, one obtains a pore size distribution centered at ~30 nm based on the adsorption branch and at ~20nm based on the desorption branch (Table 1), although with a larger distribution of pore sizes for the thicker film. Such values are in good agreement with SEM microscopy observation.

Electrochemical characterization of the EISA-SnO_2 films

The electrochemical behavior of the 100- and 250-nm thick EISA-SnO_2 films was investigated by cyclic voltammetry in a buffered aqueous solution at pH 7 (in the presence of 0.3 M KCl). As shown on the cyclic voltammograms (CVs) in Figure 2, the capacitive current density recorded at E > 0.2 V (*vs.* Ag/AgCl) remains low and independent of the applied potential. In this

potential window, the SnO_2 film behaves as an insulating porous layer as the applied potential remains much more positive than the conduction band potential of SnO_2, the latter being estimated as E_{CB} = -0.39 V at pH = 7.0 according to the following relationship (in V *vs.* Ag/AgCl):[3]

$$E_{CB} = 0.02 - 0.059\ pH \quad (1)$$

As a result, at potentials $E > 0.2$ V, the observed background current only arises from the electrical double-layer charging capacitance of the underlying exposed conductive ITO substrate. As the potential is progressively downshifted to cathodic values, *i.e.* for $E < 0.2$ V, the cyclic voltammograms (CVs) are characterized by an exponential increase of the current density which varies proportionally to the scan rate (Figure 2). This behavior is analogous to that previously described for electrodes prepared from randomly sintered SnO_2 nanoparticles.[16] This is also similar to that reported for mesoporous TiO_2 electrodes prepared either from randomly sintered nanoparticles or EISA, except that with this metal oxide the exponential growth of current occurs at significantly lower potential values (~ 0.4 V more negative) at the same pH.[19,26,27] The exponential increase of current as the applied potential is downshifted toward the conduction band potential of SnO_2 is characteristic of the progressive filling of electronic states present in the semi-conductive mesoporous material (i.e., the filling of bulk or surface localized states that are distributed in the sub-bandgap region of SnO_2 and the filling of extended conduction band states when the potential is raised close to E_{CB}). This current transition corresponds thus to the chemical capacitive charging current resulting from the exponential growth of conductivity within the semiconductive mesoporous SnO_2 film. This is finally only when the applied potential is sufficiently lower than the conduction band potential (i.e., at $E < E_{CB}$ = - 0.39 V at pH 7.0), that the semiconductive material is expected to turn out fully degenerate and so to behave as a

metal-like conductive film. Under this condition, the capacitive background current should become theoretically constant and independent of the potential (because just governed by the charging of the double-layer generated at the quasi-metallic EISA-SnO_2 film). This is however not what we can observe in Figure 2 where the current density tends to slowly increase with the rise of potential and even to become no more proportional to the scan rate at the highest cathodic potentials. This behavior can be attributed to some faradaic contribution to the current, arising most likely from slow proton intercalation as we have recently demonstrated to occur in TiO_2 electrodes under similar buffered aqueous conditions.[28]

Whatever the reason for the lack of a constant capacitive background current at potential values lower that E_{CB}, the good overlap of CVs normalized to v shown in Figure 2 for the different EISA-SnO_2 electrodes unambiguously demonstrates that the electron transport throughout the mesoporous network is not rate limiting within the range of scan rate investigated (up to 1 $V \cdot s^{-1}$). In addition, the chemical capacitive current determined at -0.35 V is observed to linearly scales with the film thickness (the current is 2.15 times larger at the 250-nm-thick EISA-SnO_2 electrode than at the 100-nm-thick, see Figure 2), a result which tends to demonstrate that the nanoporous film is structurally quite homogeneous normal to the underlying ITO surface.

The above analysis of the capacitive current of EISA-SnO_2 electrodes finally allows us to define the potential windows at pH 7.0 where the semiconductive film is switched from a poorly conductive material to a metal-like conductive material with the applied potential (see Figure 2):

- for $E > 0.2$ V, the SnO_2 semiconductive film remains insulating and the capacitance arises exclusively from the underlying exposed conductive ITO interface;

- for E_{CB} = -0.39 V < E < 0.2 V, the conductivity of the film is exponentially increased as the potential is downshifted by progressively filling the electronic states;

- for $E < E_{CB}$, the SnO_2 film is fully degenerated and behaves as a high specific surface area quasi-metallic electrode.

It is worth to note that localized surface states originating from structural defects at the SnO_2 surface are generally reported in the electronic description of mesoporous SnO_2-based electrodes.[18] It is commonly assumed that these surface states are energetically located below the conduction band, in an exponential distribution of localized states within the bandgap and also sometime characterized by a narrow distribution of monoenergetic electronic states leading to a small reversible capacitive peak located on CVs at the beginning of the transition from an insulating to conductive state. However, the capacitive current recorded with our EISA-SnO_2 electrodes does not allow to clearly identify such monoenergetic surface states, even though a small shoulder is visible at ~0.06 V (*vs.* Ag/AgCl) on the CVs of Figure 2 (especially for the 250-nm thick EISA-SnO_2 electrodes) as in other studies.[16]

Spectroelectrochemical characterization of EISA-SnO_2 films functionalized by redox-active chromophores.

The 250-nm-thick EISA-SnO_2 electrodes were chemically functionalized by FMN and OsP (see Scheme S1 for molecular structures) through chemisorption of these compounds onto the metal oxide surface (on account of the presence of an organophosphorous anchoring group, the FMN and OsP compounds are able to strongly chemisorb onto the SnO_2 surface through a similar heterocondensation reaction than that previously demonstrated at ITO surfaces[29]). These two molecules were selected because of (i) their intense redox-dependent visible absorption features

(ii) sufficiently different formal reduction potentials ($E^{0'}_{FMN}$= -0.4 V and E^{0}_{OsP} = 0.6 V vs Ag/AgCl) so that in the case of FMN it lies close to the E_{CB} of SnO_2 while for OsP it locates at a potential window where SnO_2 is insulating, and (iii) their ability to rapidly and reversibly exchange electrons at a conductive interface.

After careful rinsing, the resulting modified electrodes were characterized by real-time UV-visible absorption spectroelectrochemistry in a buffer solution. This methodology allows for monitoring selectively the absorbance changes generated by an adsorbed redox-active chromophore during the time course of a cyclic voltammetry experiment, leading thus to the establishment of cyclic voltabsorptograms (CVAs) at specific wavelengths. Time derivative of CVAs allows for derivative cyclic voltabsorptograms (DCVAs), which are equivalent to the simultaneously recorded cyclic voltammograms but without the capacitive current contribution.[30] Consequently, CVAs and DCVAs allow for a more specific and accurate monitoring of electron transfer reactions with adsorbed redox chromophores than CVs, for which the huge capacitive contribution at negative potentials tends to mask the faradaic response.[19]

During a CV scan, reduction/oxidation of the adsorbed redox chromophore can occur through one or a combination of the following three electron transport mechanisms:

(1) by physical diffusion of the redox probe throughout the void volume of the mesoporous film up to the underlying conductive ITO electrode, a process that is however here assumed to be unlikely on account of the strong chemisorption of redox chromophores we have selected. The strong anchoring of FMN or OsP to the SnO_2 metal oxide surface was asserted by the good stability of the resulting modified electrodes, even under prolonged immersion in a high

ionic strength aqueous buffer (desorption of the redox-active molecules has been observed to be less than 8% / hour);

(2) by a diffusion-like electron transport from the underlying conductive ITO electrode through electron hopping between adjacent redox probes, a phenomenon that is well-known in insulating films loaded with high surface coverages of redox-active molecules.[31]

(3) by direct heterogeneous electron transfer at the SnO_2 interface when the Fermi level of electrons in the metal oxide film (or film conductivity) is raised sufficiently negative (i.e. by scanning the potential in CV at sufficiently cathodic values).

A first set of experiments was conducted at pH 7.0 at a FMN-SnO_2 electrode by monitoring the current as well as the absorbance change at 450 nm during the time-course of a cyclic voltammogram performed from -0.1 to -0.6 V (*vs.* Ag/AgCl). As shown in Figure 3, the CV is characterized by a pair of well-defined symmetric waves centered at -0.4 V, a value that corresponds to the formal potential of the two-electrons redox transition of FMN at pH 7 in homogeneous solution.[32,33] The current intensity of the CVs is also proportional to the scan rate, up to v = 0.1 $V \cdot s^{-1}$ (Figure S4), characteristic of conductive surface-confined redox-active species. From integration of both cathodic and anodic peaks, a FMN surface coverage of ca. 0.6 $nmol \cdot cm^{-2}$ (normalized to the geometric electrode area) could be estimated when assuming a 2-electron redox transition. This value is consistent with that calculated from the absorbance change monitored at 450 nm on the CVA of Figure 3, assuming $\Delta\varepsilon_{450}$ ~10 000 $M^{-1} \cdot cm^{-1}$. The full reversibility and lack of hysteresis in the CVA is also coherent with the low ΔE_p value observed on the CV (ΔE_p < 30 mV), demonstrating that the reversible reduction of the chemisorbed FMN occurs under thermodynamic equilibrium within the range of scan rates investigated. The redox

behavior of FMN on SnO_2 is very similar to that reported on ITO,[33] a behavior which implies not only fast interfacial proton-coupled electron transfer reactions at the metal oxide interface, but also fast electron transport throughout the 250-nm-thick semiconductive SnO_2 network. This also entails that the EISA-SnO_2 electrode behaves as a metal-like electrode within the potential window corresponding to the FMN redox transition (Figure 3). A similar reversible electron transfer mechanism is also obtained for EISA-SnO_2 electrodes modified with microperoxidase 11 (MP-11, Figure S5), a one-electron transfer redox chromophore characterized by a standard potential close to that of FMN ($E^0_{MP\text{-}11}$ = -0.37 V) and that easily physisorbs within the mesoporous SnO_2 film (see Scheme S1). This result clearly shows that a reversible interfacial electron transfer can be expected as long as (i) the redox potential of the chemisorbed redox compound lies close or more negative to the conduction band potential of SnO_2 and (ii) the redox compound allows for a fast and reversible electron transfer reaction, independent of the nature of interactions the redox molecule has with the metal oxide surface. It is interesting to note that in contrast to the reversible wave we observed here for MP-11 in EISA-SnO_2, an irreversible CV peak was previously reported for the same molecule in EISA-TiO_2 films.[19] This distinctive behavior is fully consistent with a conduction band potential of TiO_2 that is ~0.4 V more negative than SnO_2.[3]

Similar experiments were next conducted at the OsP-functionalized SnO_2 electrodes. As the standard potential of the OsP complex (E^0_{OsP} = 0.6 V) lies in a potential window where SnO_2 is insulating, it can be anticipated that direct interfacial electron transfer between SnO_2 and OsP should proceed irreversibly once the potential applied to the SnO_2 film is sufficiently negative to convert the latter reasonably conductive (*i.e.* for $E < 0.2$ V at pH 7). Since the osmium complex we have used to prepare the functionalized electrode was the reduced form, before performing

any cathodic CV or CVA scan it was first necessary to in situ convert the chemisorbed complex in its oxidized form. This has been rendered possible thanks to the application of a constant preconditioning anodic potential (E = 1.0 V) to the OsP-functionalized SnO_2 film for at least 30 seconds (see Figures S6). Under these conditions, even though the SnO_2 material remains insulating, the electrochemical oxidation of the Os^{II} complex is expected to proceed most likely by a slow electron hopping between adjacent redox-active molecules. This slow oxidation process is supported by the fact that the time needed to fully oxidize the chemisorbed OsP complex contained within the 250-nm thick SnO_2 electrode (i.e. ~30 s) is relevant of an apparent slow diffusion coefficient D of $\sim 7\times10^{-12}$ $cm^2 \cdot s^{-1}$ (assuming a diffusion length of $l = (\pi D t)^{1/2}$). Such a low value is in agreement with a poorly efficient hopping electron transport between adjacent adsorbed molecules. From the total absorbance change in Figure S6, a total surface coverage Γ^0 of 2.2 $nmol \cdot cm^{-2}$ can be estimated for the grafted OsP complex (using an extinction coefficient of 12000 $M^{-1} \cdot cm^{-1}$, as usually reported for osmium tris-bipyridine complexes in water).[34] This surface coverage (normalized to the geometric electrode area) is significantly much larger than that obtained with the FMN chromophore, a difference that can be related to the lower reactivity of phosphate compared to phosphonate anchoring groups toward chemisorption on metal oxide surfaces.[29]

Once converted to its oxidized form, the OsP-modified SnO_2 electrode was then characterized in cyclic voltabsorptommetry by monitoring the absorbance change at 485 nm. Resulting CVs and CVAs are reported in Figure 3. Their shapes strongly differ from those obtained at the FMN-functionalized SnO_2 electrode. Indeed, reduction of the Os^{III} complex appears as a biphasic process. A first reversible wave centered on the standard potential of the Os^{III}/Os^{II} redox couple (E^0 = 0.6 V) is observed at a potential where SnO_2 is insulating, leading to the reduction of a

fraction of the total amount of adsorbed OsP complex (that only a fraction of OsP is reduced during this first reduction wave is clearly evident from the absorbance change as a function of potential, and it can be estimated to correspond to a fraction of ~50% at the scan rate of 0.05 V s^{-1}). The remaining fraction of adsorbed OsP complex is thereafter fully reduced at more negative potential, leading to an irreversible reduction peak localized at 0.03 V. By comparing the CVs at different scan rates in figure S7, it can be concluded that the first reversible process is a diffusion-like process as its intensity is proportional to the square root of the scan rate. From the cathodic peak intensity of this reversible process, an apparent diffusion coefficient of ~10^{-11} $cm^2 \cdot s^{-1}$ can be estimated if assuming a starting volumic film concentration of 9×10^{-5} $mol \cdot cm^{-3}$ OsP within the 250-nm thick film (calculated from the geometric surface concentration of 2.2 nmol cm^{-2} OsP).

This biphasic reduction process is reminiscent to that previously reported at mesoporous EISA-TiO_2 electrodes functionalized by an iron porphyrin.[19] It is indicative of the co-existence of two charge transfer mechanisms: a first diffusion-like mechanism involving most likely electron hopping transport between adjacent chemisorbed OsP complexes across the insulating SnO_2 network, and a second mechanism involving direct interfacial electron transfer from SnO_2 to the oxidized adsorbed molecule. This second mechanism is only efficient once a significant concentration of electrons is injected into the semiconductive material (i.e., at $E < 0.2$ V at pH 7.0).

Quantitative analysis of this irreversible reduction process was performed on the derivative cyclic voltabsorptograms (DCVAs) recorded at different scan rates and pH, and represented as flux of molecules transformed (Φ in $mol \cdot cm^{-2} \cdot s^{-1}$) as a function of potential using eq 2:

$$\phi = -\frac{1}{1000.\Delta\varepsilon_{485}}\frac{vdA_{485}}{dE} \quad (2)$$

where $\Delta\varepsilon_{485}$ corresponds to the variation of the extinction coefficient between the two redox states of the osmium complex at 485 nm (i.e., 12000 $mol^{-1}\cdot L\cdot cm^{-1}$).

The experimental DCVAs recorded at pH 5 and different scan rates ranging from 10 to 500 $mV\cdot s^{-1}$ are given in Figure 4 and S8 (only the forward cathodic scan is shown). It can be seen in Figure 4 that the amplitude of the total absorbance change is independent of the scan rate, indicating full redox conversion of the Os^{III} at the end of the forward cathodic scan whatever the scan rate, while the shapes of CVAs and DCVAs show strong dependence on the scan rate. At low scan rates, reduction of Os^{III} is a biphasic process as described above, and the two successive reduction peaks on the DCVA correspond to (i) a first reversible Os^{III} reduction through a diffusion-controlled process located within a potential window where SnO_2 is insulating, followed by (ii) a second irreversible Os^{III} reduction through an interfacial electron transfer from SnO_2 to the adsorbed complex at a potential where SnO_2 is becoming increasingly conductive. As the scan rate is increased (and thus the time window of the CV decreased), the fraction of adsorbed Os^{III} reduced through the first diffusion mechanism is progressively decreased, while during the second irreversible electron transfer mechanism almost all of the remaining adsorbed Os^{III} molecules are reduced, even at the highest scan rates.

In order to get deeper insights into the heterogeneous electron transfer between SnO_2 and the chemisorbed Os^{III} redox probe, the second irreversible wave was analyzed by assuming the following electron transfer/transport mechanism (same mechanism as previously proposed for TiO_2[19]):

(1) $e^- + \square_{SnO2} \leftrightarrows e^-_{SnO2}$ (E_{CB}, α, C_e^0)

(2) $e^-_{SnO2} + Os^{III} \rightarrow Os^{II}$ (k)

The first equation is related to the fast electron injection from the underlying conductive ITO surface to an exponential distribution of electronic states of SnO_2 (i.e., a Boltzmann distribution of empty conduction band electronic states completed by the potential contribution of an exponential distribution of empty surface states localized in the bandgap), followed by fast transport of the injected electrons e^-_{SnO2} through a random walk diffusion-like process across the SnO_2 mesoporous network (so fast that it can be assumed as being not rate limiting, see above). In this description, C_e^0 is the maximal concentration of electrons that can be injected at saturation in the SnO_2 material and the parameter α is a dimensionless factor that characterizes the energy distribution of electronic states involved in the interfacial electron transfer. An α value of 1 indicates that only electrons from the conduction band are involved in the heterogeneous electron transfer, while an α value < 1 indicates a significant contribution of the lower energy surface electronic states to the interfacial electron transfer.[19]

The second equation is related to the irreversible interfacial electron transfer reaction between the adsorbed Os^{III} species and the electrons at the SnO_2 film/solution interface, wherein k is an average value of the interfacial electron transfer rates characterizing the different electronic states involved in the electron transfer. In the limiting case for which electron diffusion throughout the semi-conductive network is not interfering in the kinetics, the irreversible reduction wave can be described by the following analytical expression (see SI for details):

$$\phi = kC_e^0 \Gamma exp\left[-\alpha \frac{F}{RT}(E - E_{\mathrm{CB}})\right] exp\left(-\frac{RT}{\alpha F v} kC_e^0 exp\left[-\alpha \frac{F}{RT}(E - E_{\mathrm{CB}})\right]\right) \qquad (3)$$

where E is the applied potential (in V), T the temperature (in K), F the Faraday constant (96500 $C \cdot mol^{-1}$), R = 8.314 $J \cdot K^{-1} \cdot mol^{-1}$, and Γ the surface coverage of the oxidized form of adsorbed redox chromophore directly reduced at the SnO_2 interface (in $mol \cdot cm^{-2}$). In the present case, Γ is function of the scan rate as partial reduction of the total amount of adsorbed Os^{III} , i.e. Γ^0, can occur by an electron hoping when E is close to E^0_{OsP}. Consequently, we can define (1-f) the fraction of redox probe reduced during the first diffusion-controlled reduction step and f the fraction of Os^{III} reduced during the second irreversible reduction step. The Γ value in eq 3 is thus given by the product $f \times \Gamma^0$.

The analytical expression for the peak potential position of the irreversible wave is given by eq 4:

$$E_P = E_{CB} + \frac{RT}{\alpha F} ln\left(\frac{RT}{\alpha F}\frac{kC_e^0}{v}\right) \quad (4)$$

The peak potential of the irreversible wave was shown to linearly vary with the logarithm of scan rate (Figure 5). From a linear regression fit of the experimental data and by assuming E_{CB} = -0.27 V at pH 5 using eq 1, values of α = 0.71 and kC_e^0 = 1.2×10^5 s^{-1} could be recovered. These parameters were then used in eq 3 to calculate the DCVAs at pH 5 in the range of 10 to 500 $mV \cdot s^{-1}$ (Figures 4 and S4). The fraction f of Os^{III} reduced directly at the SnO_2 interface was fixed to adjust the intensity of the simulated irreversible wave.

Similar experiments were also conducted at pH 7 and 8.5 using the same Os-SnO_2 electrode. The resulting DCVAs and CVs recorded at 0.05 $V \cdot s^{-1}$ are plotted in Figure 5. As the pH was raised up, the irreversible wave was progressively shifted to lower potentials, consistent with the downshift of SnO_2 conduction band potential with the pH. The scan rate dependence of the peak

potential was analyzed according to eq 4, taking into account the pH-dependence of E_{CB} according to eq 1. The resulting data showed in Figure 5 overlay with that obtained at pH 5, and clearly demonstrate that α as well as $kC_e^{\,0}$ are almost unaffected by pH.

The very good fitting of eqs 3 and 4 to the experimental data demonstrates that our simple model, initially developed for mesoporous EISA-TiO_2 electrodes,[19] can be extended to other semi-conductive materials to extract the important parameters related to the interfacial electron transfer between an adsorbed redox dye and the semi-conductive material. It has to be noticed that in contrast to our previous work done with EISA-TiO_2, the DCVA recorded up to 0.5 $V{\cdot}s^{-1}$ are not affected by ohmic drop. This is mainly due to the use of a higher ionic strength buffer solution than previously, which is made possible thanks to the strong chemisorption of the phosphonate osmium complex on SnO_2, leading therefore to a high stability of the functionalized electrodes toward desorption.

Some comments can be made on the two parameters α and $kC_e^{\,0}$ characterizing the interfacial electron transfer between SnO_2 and the adsorbed Os^{III} complex. First of all, the α value of 0.71 indicates that the electrons involved in the interfacial electron transfer arise from a larger energy distribution of electronic states than those of the conduction band, meaning thus that low-energy electronic surface states distributed in the bandgap are involved in the interfacial electron transfer. This result significantly differs from that we have previously obtained at EISA-TiO_2 electrodes for which a α value of 1 was found, characteristic of a heterogeneous electron transfer reaction involving exclusively the extended conduction band states (Figure 6) but not the electrons trapped in the low-energy states within the bandgap of TiO_2 (the latter can only be indirectly involved through an equilibrated bulk trapping-detrapping mechanism with the

extended conduction band states).[26] An explanation we had put forward to interpret this lack of electron transfer communication with localized traps in TiO_2 is that the traps are predominantly located into the bulk of EISA-TiO_2 rather than on the surface of the metal oxide material.[19] In the present case of EISA-SnO_2 electrodes, a α value lower than one thus suggests that a significantly higher number of surface traps are present, contributing thus to a wider energy range to the interfacial electron transfer and so to an enlargement of the irreversible reduction peak in CV or DCVA. These observations are in line with several reports highlighting the role of the surface localized states in the faster recombination rates in dye-sensitized solar cells made of nanoparticulate films of SnO_2 as compared to those made of TiO_2.[16–18] In the present work, we moreover demonstrate that the α value is independent of the pH, a result which indicates that the low-energy surface states distribution follow the same pH-dependence as for the conduction band potential.

The second parameter kC_e^0 describes an apparent first order interfacial electron transfer rate wherein k corresponds in fact to an average value between the different electron transfer rates arising from both the conduction band states and the localized surface states. Knowing the value of C_e^0 would allow extracting the average value k from kC_e^0, but because the information on the density of electronic states and their distribution in the EISA-SnO_2 film is not available, this has not been achieved. Interestingly, kC_e^0 shows no significant dependence on pH, which most likely indicates that the average value of k is almost pH-independent (if one assumes that C_e^0 is essentially a function of the intrinsic structural properties of the film). This result is reminiscent of the observation made by Hupp *and coll.,* showing that electron transfer from the conduction band of TiO_2 to a ruthenium complex is pH-independent over 19 pH unit range.[35,36] Such

independence of electron transfer rate with pH variation suggests that electron transfer at the SnO_2 interface is decoupled from any proton transfer. While the potential of SnO_2 electronic states is pH-dependent and that of the OsP redox couple is not, it is tempting to link the pH-independent electron transfer rate to a pH-dependent driving force for the reaction by assuming that the electron energy is equivalent to the conduction band energy. This assumption should however only be valid for a proton-coupled interfacial electron transfer reaction, which is apparently not the case in the present study on account of the pH-independence of the electron transfer rate. Assuming here a pure electron transfer at the interface, it is therefore no more possible to define the proper energy of the transferred electron as it is not defined by the pH-dependent conduction band potential. The actual average driving force for interfacial electron transfer from SnO_2 to a redox couple cannot be evaluated and thus remains an open question. As a consequence it appears that more insights into the proton-coupled energetics of metal oxide semiconductor electrodes are required to characterize electron transfer between such electrodes and redox couples in terms of intrinsic parameters such as reorganization energies and pre-exponential factors as in the Marcus-Gerischer equation.[37]

CONCLUSION

In the present work, we prepared highly-ordered crystalline mesoporous SnO_2 electrodes by EISA with large pores and adjustable thicknesses by taking advantage of the two deposition regimes allowed by the dip-coating process. The thicker electrodes were then chemically modified by two redox-active chromophores allowing us to investigate the heterogeneous electron transfer at the SnO_2 interface to gain better insights into the reactive electronic states involved. Quantitative analysis of the spectroelectrochemical results was achieved in the

theoretical framework initially developed for mesoporous TiO_2 electrodes demonstrating thus that it can be successfully extended to other semi-conductive materials. Our results unambiguously evidence that the interfacial electron transfer at the SnO_2 interface involves not only the extended conduction band states, but also the localized lower-energy electronic states present at the SnO_2/aqueous electrolyte interface. This significantly differs from our previous results at EISA-TiO_2 electrodes, wherein the interfacial electron transfer was shown to only involve the extended conduction band states. Accordingly, EISA–SnO_2 electrodes exhibit a specific interfacial electron–transfer reactivity related to the presence of sub-band gap surface states electronically-coupled to the adsorbed redox-active molecules.

ASSOCIATED CONTENT

Supporting Information. Details of the theoretical framework developed to analyze interfacial electron transfer at semi-conductive SnO_2 interface, Molecular structure of the redox probes, characterization of the EISA-SnO_2 electrodes prepared by thermo-ellipsommetry, X-ray diffraction, gas adsorption/desorption. Complementary CVs, CVAs and DCVAs at modified EISA-SnO_2 electrodes.

AUTHOR INFORMATION

Corresponding Author

veronique.balland@univ-paris-diderot.fr

Author Contributions

The manuscript was written through contributions of all authors. All authors have given approval to the final version of the manuscript.

Acknowledgements

This work was supported by the Agence Nationale pour la Recherche (ANR 3D-BIOELEC).

REFERENCES

(1) Alibabaei, L.; Luo, H.; House, R. L.; Hoertz, P. G.; Lopez, R.; Meyer, T. J. Applications of Metal Oxide Materials in Dye Sensitized Photoelectrosynthesis Cells for Making Solar Fuels: Let the Molecules Do the Work. *J. Mater. Chem. A* **2013**, *1*, 4133.

(2) Wali, Q.; Fakharuddin, A.; Jose, R. Tin Oxide as a Photoanode For Dye-Sensitised Solar Cells: Current Progress and Future Challenges. *J. Power Sources* **2015**, *293*, 1039–1052.

(3) Bolts, J. M.; Wrighton, M. S. Correlation of Photocurrent-Voltage Curves with Flat-Band Potential for Stable Photoelectrodes for the Photoelectrolysis of Water. *J. Phys. Chem.* **1976**, *80*, 2641–2645.

(4) Green, A. N. M.; Palomares, E.; Haque, S. A.; Kroon, J. M.; Durrant, J. R. Charge

Transport versus Recombination in Dye-Sensitized Solar Cells Employing Nanocrystalline TiO_2 and SnO_2 Films. *J. Phys. Chem. B* **2005**, *109*, 12525–12533.

(5) Zhang, M.; Chen, C.; Ma, W.; Zhao, J. Visible-Light-Induced Aerobic Oxidation of Alcohols in a Coupled Photocatalytic System of Dye-Sensitized TiO_2 and TEMPO. *Angew. Chemie* **2008**, *120*, 9876–9879.

(6) Song, W.; Vannucci, A. K.; Farnum, B. H.; Lapides, A. M.; Brennaman, M. K.; Kalanyan, B.; Alibabaei, L.; Concepcion, J. J.; Losego, M. D.; Parsons, G. N. et al. Visible Light Driven Benzyl Alcohol Dehydrogenation in a Dye-Sensitized Photoelectrosynthesis Cell. *J. Am. Chem. Soc.* **2014**, *136*, 9773–9779.

(7) Milot, R. L.; Moore, G. F.; Crabtree, R. H.; Brudvig, G. W.; Schmuttenmaer, C. A. Electron Injection Dynamics from Photoexcited Porphyrin Dyes into SnO_2 and TiO_2 Nanoparticles. *J. Phys. Chem. C* **2013**, *117*, 21662–21670.

(8) Milot, R. L.; Schmuttenmaer, C. A. Electron Injection Dynamics in High-Potential Porphyrin Photoanodes. *Acc. Chem. Res.* **2015**, *48*, 1423–1341.

(9) Tiwana, P.; Docampo, P.; Johnston, M. B.; Snaith, H. J.; Herz, L. M. Electron Mobility and Injection Dynamics in Mesoporous ZnO, SnO_2, and TiO_2 Films Used in Dye-Sensitized Solar Cells. *ACS Nano* **2011**, *5*, 5158–5166.

(10) Kamat, P. V; Bedja, I.; Hotchandani, S.; Patterson, L. K. Photosensitization of Nanocrystalline Semiconductor Films. Modulation of Electron Transfer between Excited Ruthenium Complex and SnO_2 Nanocrystallites with an Externally Applied Bias. *J. Phys. Chem.* **1996**, *100*, 4900–4908.

(11) Huang, J.; Stockwell, D.; Boulesbaa, A.; Guo, J.; Lian, T. Comparison of Electron Injection Dynamics from Rhodamine B to In_2O_3 , SnO_2 , and ZnO Nanocrystalline Thin Films. *J. Phys. Chem. C* **2008**, *112*, 5203–5212.

(12) Godin, R.; Sherman, B. D.; Bergkamp, J. J.; Chesta, C. A.; Moore, A. L.; Moore, T. A.; Palacios, R. E.; Cosa, G. Charge-Transfer Dynamics of Fluorescent Dye-Sensitized Electrodes under Applied Biases. *J. Phys. Chem. Lett.* **2015**, *6*, 2688–2693.

(13) Asbury, J. B.; Hao, E.; Wang, Y.; Ghosh, H. N.; Lian, T. Ultrafast Electron Transfer Dynamics from Molecular Adsorbates to Semiconductor Nanocrystalline Films. **2001**, *105*, 4545.

(14) Anderson, N. A.; Lian, T. Ultrafast Electron Transfer At the Molecule-Semiconductor Nanoparticle Interface. *Annu. Rev. Phys. Chem.* **2005**, *56*, 491–519.

(15) Bergeron, B. V; Marton, A.; Oskam, G.; Meyer, G. J. Dye-Sensitized SnO_2 Electrodes with Iodide and Pseudohalide Redox Mediators. *J. Phys. Chem. B* **2005**, *109*, 937–43.

(16) Knauf, R. R.; Brennaman, M. K.; Alibabaei, L.; Norris, M. R.; Dempsey, J. L. Revealing the Relationship between Semiconductor Electronic Structure and Electron Transfer Dynamics at Metal Oxide–Chromophore Interfaces. *J. Phys. Chem. C* **2013**, *117*, 25259–25268.

(17) Prasittichai, C.; Hupp, J. T. Surface Modification of SnO_2 Photoelectrodes in Dye-Sensitized Solar Cells: Significant Improvements in Photovoltage via Al_2O_3 Atomic Layer

Deposition. *J. Phys. Chem. Lett.* **2010**, *1*, 1611–1615.

(18) Huang, Q.; Li, F.; Gong, Y.; Luo, J. Recombination in SnO_2-Based Quantum Dots Sensitized Solar Cells: The Role of Surface States. *J. Phys. Chem. C* **2013**, 2–10.

(19) Renault, C.; Nicole, L.; Sanchez, C.; Costentin, C.; Balland, V.; Limoges, B. Unraveling the Charge Transfer/Electron Transport in Mesoporous Semiconductive TiO_2 Films by Voltabsorptometry. *Phys. Chem. Chem. Phys.* **2015**, *17*, 10592–10607.

(20) Sakatani, Y.; Grosso, D.; Nicole, L.; Boissiere, C.; de A. A. Soler-Illia, G. J.; Sanchez, C. Optimised Photocatalytic Activity of Grid-like Mesoporous TiO_2 Films: Effect of Crystallinity, Pore Size Distribution, and Pore Accessibility. *J. Mater. Chem.* **2006**, *16*, 77–82.

(21) Brezesinski, T.; Fischer, A.; Iimura, K. I.; Sanchez, C.; Grosso, D.; Antonietti, M.; Smarsly, B. M. Generation of Self-Assembled 3D Mesostructured SnO_2 Thin Films with Highly Crystalline Frameworks. *Adv. Funct. Mater.* **2006**, *16*, 1433–1440.

(22) Grosso, D. How to Exploit the Full Potential of the Dip-Coating Process to Better Control Film Formation. *J. Mater. Chem.* **2011**, *21*, 17033.

(23) Gillaizeau-Gauthier, I.; Odobel, F.; Alebbi, M.; Argazzi, R.; Costa, E.; Bignozzi, C. A.; Qu, P.; Meyer, G. J. Phosphonate-Based Bipyridine Dyes for Stable Photovoltaic Devices. *Inorg. Chem.* **2001**, *40*, 6073–6079.

(24) Lepoutre, S.; Smått, J.-H.; Laberty, C.; Amenitsch, H.; Grosso, D.; Lindén, M. Detailed Study of the Pore-Filling Processes during Nanocasting of Mesoporous Films using SnO_2/SiO_2 as a Model System. *Microporous Mesoporous Mater.* **2009**, *123*, 185–192.

(25) Boissiere, C.; Grosso, D.; Lepoutre, S.; Nicole, L.; Bruneau, A. B.; Sanchez, C. Porosity and Mechanical Properties of Mesoporous Thin Films Assessed by Environmental Ellipsometric Porosimetry. *Langmuir* **2005**, *21*, 12362–12371.

(26) Fabregat-Santiago, F.; Mora-Seró, I.; Garcia-Belmonte, G.; Bisquert, J. Cyclic Voltammetry Studies of Nanoporous Semiconductors. Capacitive and Reactive Properties of Nanocrystalline TiO_2 Electrodes in Aqueous Electrolyte. *J. Phys. Chem. B* **2003**, *107*, 758–768.

(27) Berger, T.; Monllor-Satoca, D.; Jankulovska, M.; Lana-Villarreal, T.; Gomez, R. The Electrochemistry of Nanostructured Titanium Dioxide Electrodes. *ChemPhysChem* **2012**, *13*, 2824–2875.

(28) Kim, Y.-S.; Kriegel, S.; Harris, K. D.; Costentin, C.; Limoges, B.; Balland, V. Evidencing Fast, Massive, and Reversible H^+ Insertion in Nanostructured TiO_2 Electrodes at Neutral pH. Where Do Protons Come From? *J. Phys. Chem. C* **2017**, *121*, 10325–10335.

(29) Forget, A.; Limoges, B.; Balland, V. Efficient Chemisorption of Organophosphorous Redox Probes on Indium Tin Oxide Surfaces under Mild Conditions. *Langmuir* **2015**, *31*, 1931–1940.

(30) Bancroft, E. E.; Sidwell, J. S.; Blount, H. N. Derivative Linear Sweep and Derivative Cyclic Voltabsorptometry. *Anal. Chem.* **1981**, *53*, 1390–1394.

(31) Trammell, S. A.; Meyer, T. J. Diffusional Mediation of Surface Electron Transfer on TiO_2. *J. Phys. Chem. B* **1999**, *103*, 104–107.

(32) Mayhew, S. G. The Effects of pH and Semiquinone Formation on the Oxidation–Reduction Potentials of Flavin Mononucleotide. *Eur. J. Biochem.* **1999**, *265*, 698–702.

(33) Forget, A.; Tucker, R. T.; Brett, M. J.; Limoges, B.; Balland, V. Tuning the Reactivity of Nanostructured Indium Tin Oxide Electrodes Toward Chemisorption. *Chem. Commun.* **2015**, *51*, 6944–6947.

(34) Jung, M. C.; Munro, N.; Shi, G.; Michael, A. C.; Weber, S. G. Use of Tris(2,2‘-bipyridine)osmium as a Photoluminescence-Following Electron-Transfer Reagent for Postcolumn Detection in Capillary High-Performance Liquid Chromatography. *Anal. Chem.* **2006**, *78*, 1761–1768.

(35) Yan, S. G.; Hupp, J. T. Semiconductor-Based Interfacial Electron-Transfer Reactivity: Decoupling Kinetics from pH-Dependent Band Energetics in a Dye-Sensitized Titanium Dioxide/Aqueous Solution System. *J. Phys. Chem.* **1996**, *100*, 6867–6870.

(36) Yan, S. G.; Hupp, J. T. Energetics of Electron Transfer at the Nanocrystalline Titanium Dioxide Semiconductor/Aqueous Solution Interface: pH Invariance of the Metal-Based Formal Potential of a Representative Surface-Attached Dye Couple. *J. Phys. Chem. B* **1997**, *101*, 1493–1495.

(37) Gerischer, H. The Impact of Semiconductors on the Concepts of Electrochemistry. *Electrochim. Acta* **1990**, *35*, 1677–1699.

FIGURES

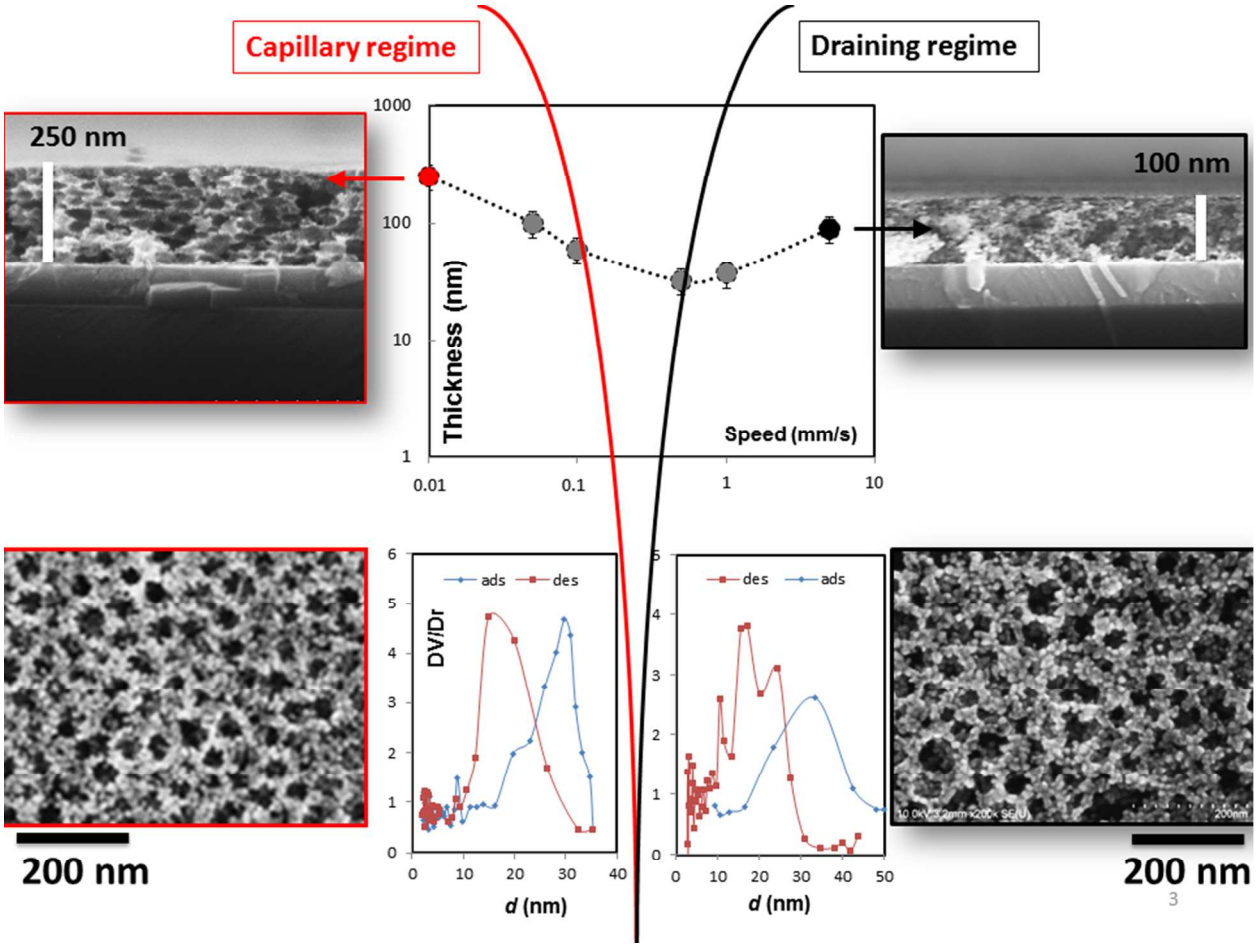

Figure 1. Cross-sectional and top SEM-FEG images of the SnO_2-films prepared at (left) 0.01 and (right) 5 $mm \cdot s^{-1}$. Middle up: film thickness (determined by ellipsometry) as a function of the dip-coating withdrawal speed. Middle down: pore size distributions calculated from adsorption/desorption isotherms.

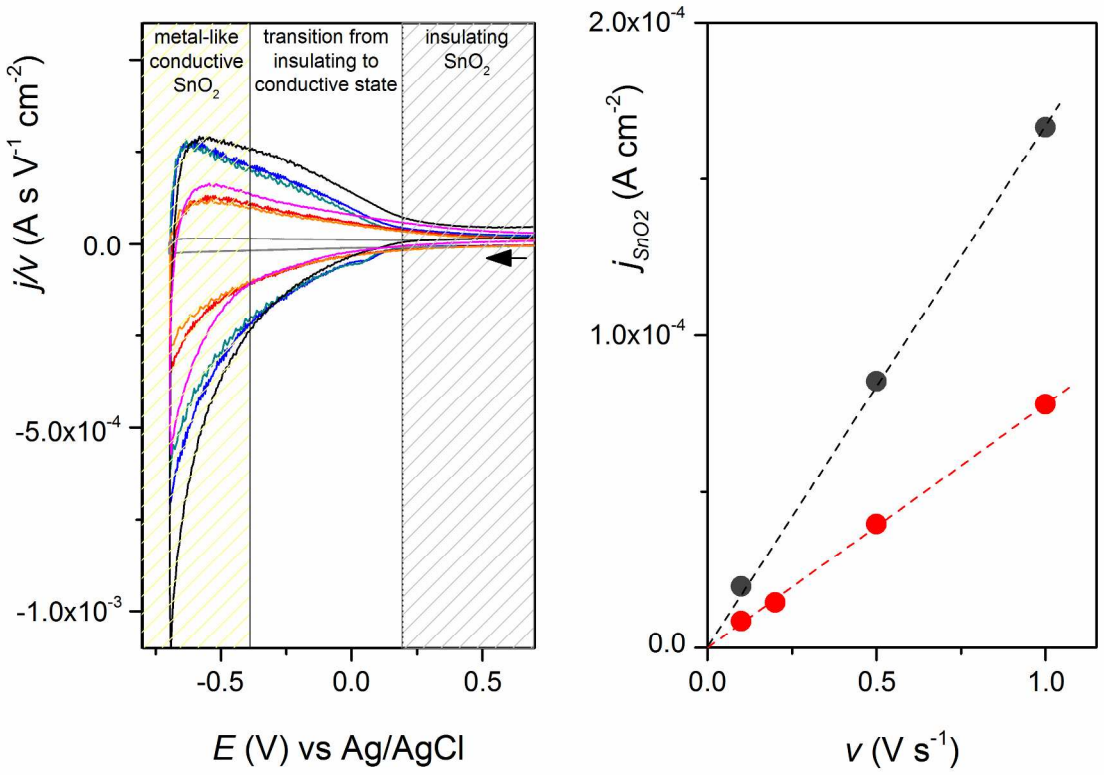

Figure 2. Left: scan rate-normalized cyclic voltammograms at (grey line) a planar ITO electrode, (magenta, red, and orange curves) a 100-nm-thick EISA-SnO_2 electrode , and (balck, blue, and green curves) a 250-nm-thick EISA-SnO_2 electrode in a Hepes aqueous buffer solution of pH 7. The three tested scan rates for each EISA-SnO_2 electrode were respectively of 0.1, 0.5 and 1 $V \cdot s^{-1}$. Right: current density determined at -0.35 V (corrected from the capacitive contribution of the underlying conductive ITO) as a function of the scan rate for the (red) 100- and (black) 250-nm EISA-SnO_2 electrode. Dashed lines correspond to the linear regression fits with slopes of 7.8×10^{-5} and 16.75×10^{-5} $A \cdot s \cdot V^{-1} \cdot cm^{-2}$ for the 100- and 250-nm EISA-SnO_2 film, respectively.

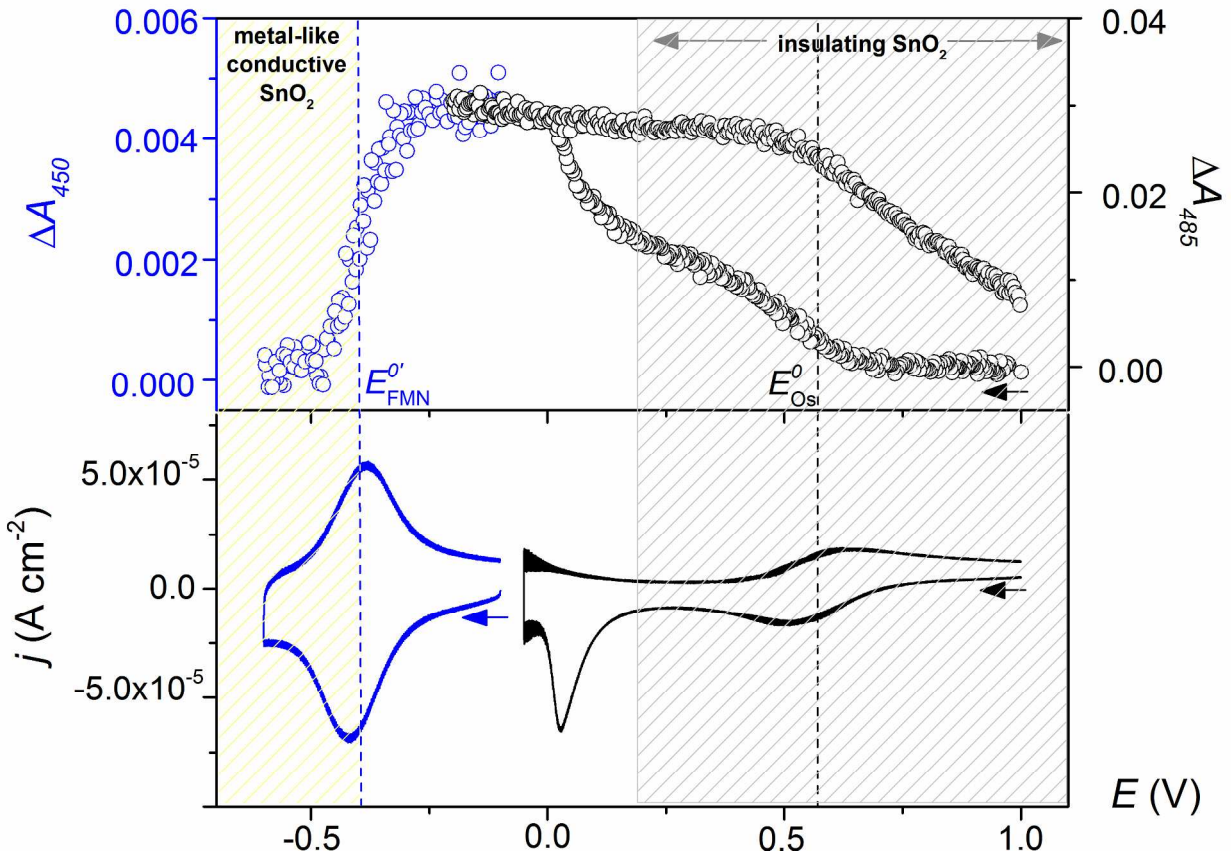

Figure 3. (Top) cyclic voltabsorptograms and (down) cyclic voltammograms recorded (v = 0.05 $V \cdot s^{-1}$) at a (blue) FMN- and (black) OsP-modified EISA-SnO_2 electrode (250 nm-thick) in a Hepes buffer (pH 7). For the CVAs, the FMN and the osmium complex were monitored at 450 nm and 485 nm, respectively. The dashed lines indicate the formal reduction potential of each redox probe in solution at pH 7.

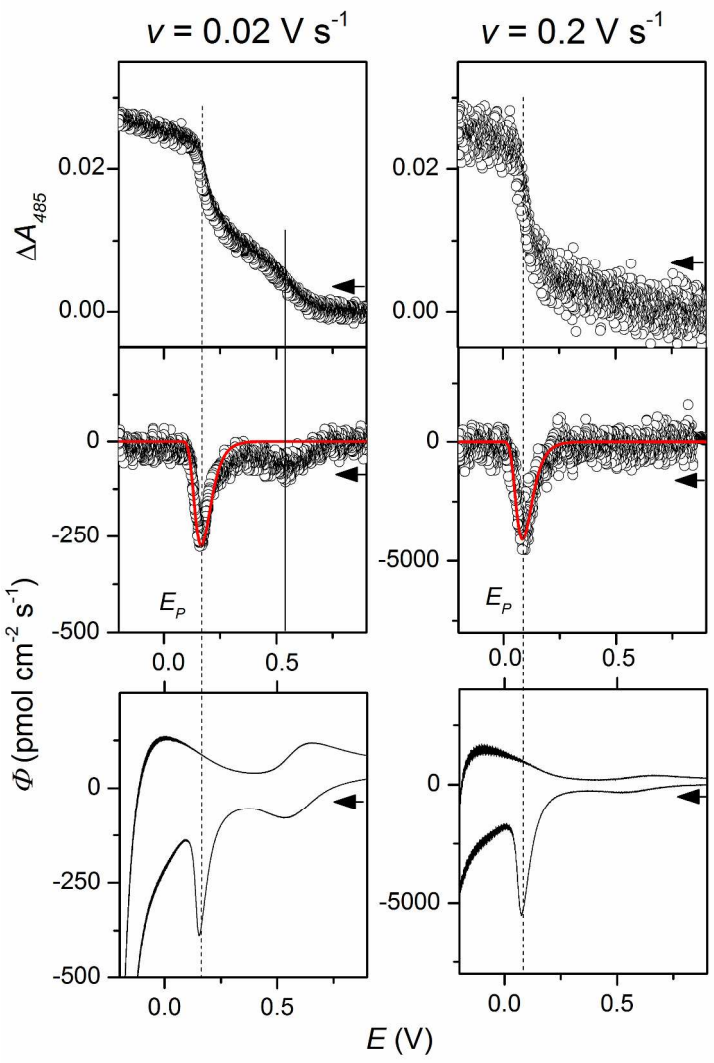

Figure 4. (Top) cathodic linear voltabsorptograms, (down) cyclic voltammograms, and (middle) cathodic derivative linear voltabsorptograms monitored at 485 nm at 0.02 or 0.2 V·s^{-1} at a OsP-modified EISA-SnO_2 electrode in a Mes buffer of pH 5 (T = 20°C, Γ^0 = 2.2 nmol·cm^{-2}). Red lines: fits of eq 3 to the experimental plots using E_{CB} = -0.27 V, α = 0.71, kC_e^0 = 1.2 10^5 s^{-1}, and f = 0.6 at 0.02 V·s^{-1} and f = 0.95 at 0.2 V·s^{-1}.

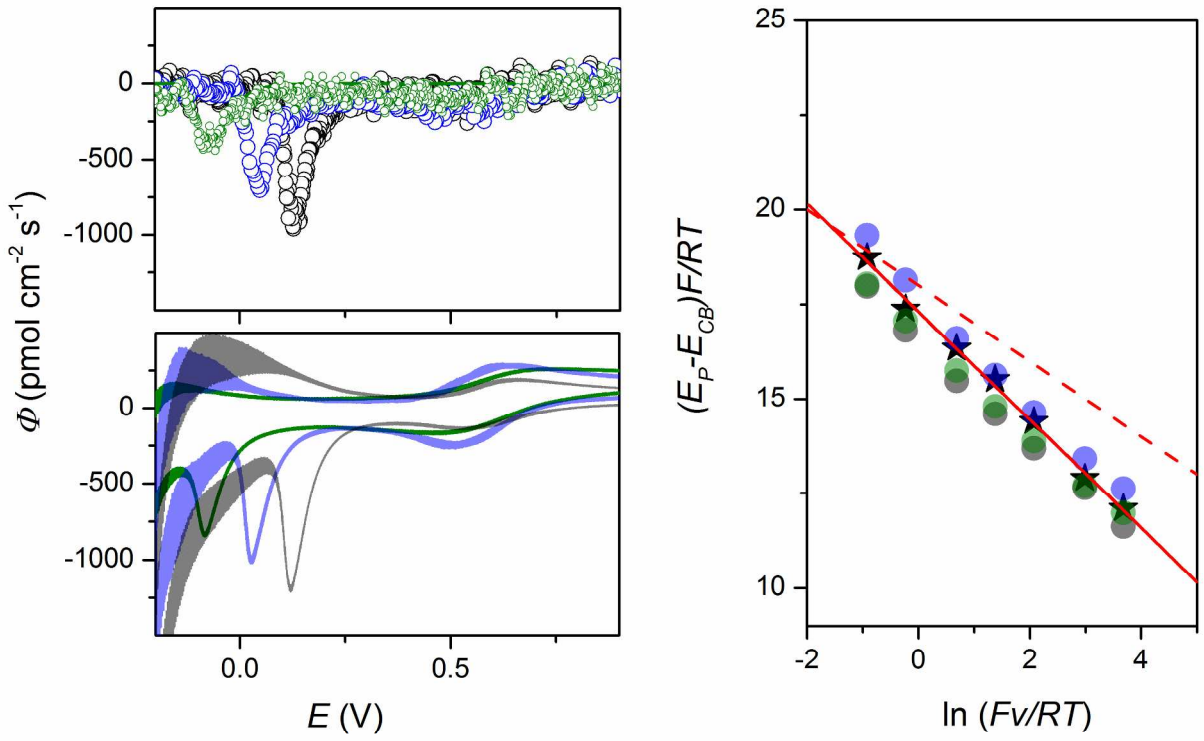

Figure 5. Left: DCVAs (top) and CVs (down) recorded at v = 0.05 V·s^{-1} at a OsP-modified EISA-SnO_2 electrode in an aqueous buffer at pH 5 (grey), 7 (blue) and 8.5 (green). Right: plot of the irreversible peak potential value obtained from CVs (●) or DCVAs (★) at pH 5 (green), 7 (blue) and 8.5 (grey) as a function of the scan rate, assuming E_{CB} = -0.27 V, - 0.39 V and -0.48 V at pH 5, 7 and 8.5, respectively (see eq 1). Plain red line: linear regression fit of eq 4 to the experimental data obtained from the DCVAs at pH 5 leading to α = 0.71 and kC_e^0 = 1.2×10^5 s^{-1}. Dashed red line: example of linear dependence with α = 1.

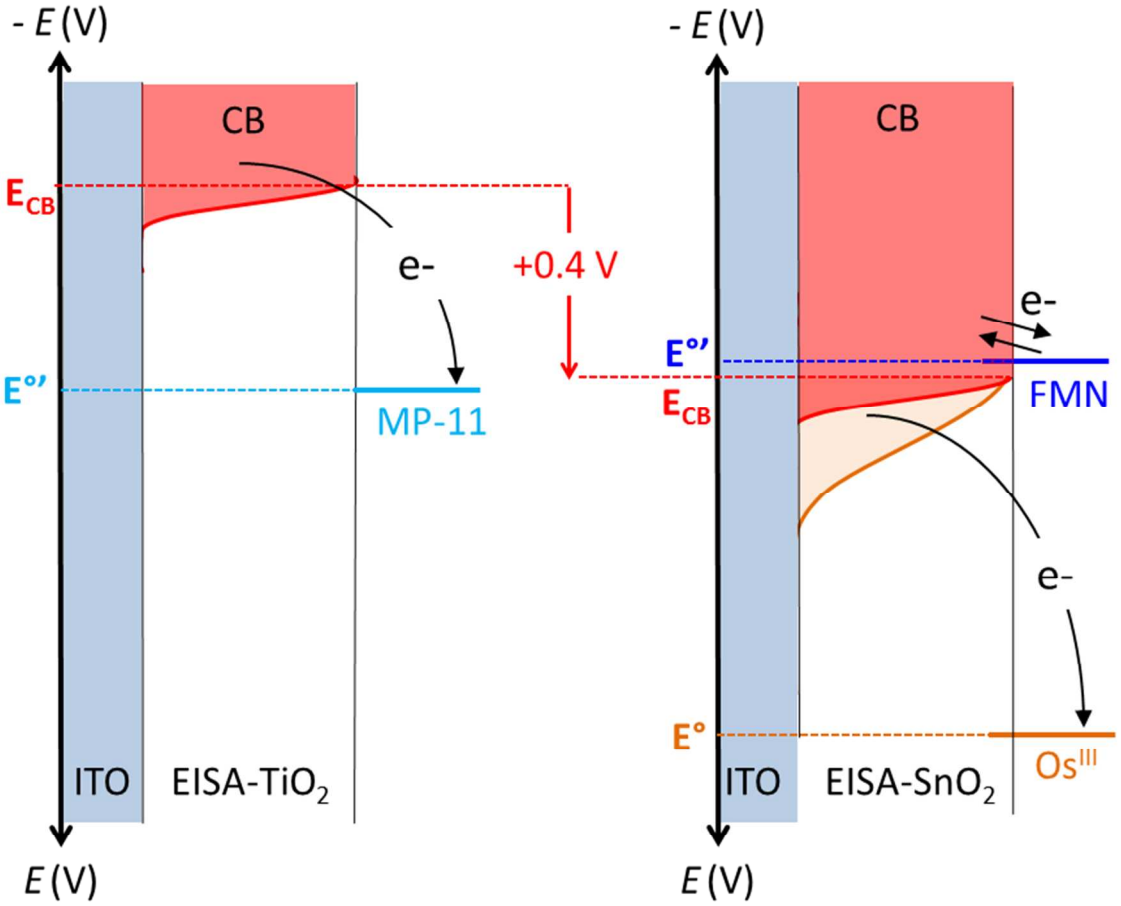

Figure 6. Schematic representations of the distribution of electronic states involved in the interfacial electron transfer between (left) EISA-TiO_2 and (right) EISA-SnO_2 semiconductive film electrodes and different adsorbed redox probes. In the case of the EISA-TiO_2 electrode, only electrons arising from the conduction band (Boltzmann distribution) are involved in the interfacial electron transfer, while for the EISA-SnO_2 electrode, low-energy electronic states localized in the band gap (exponential distribution with $\alpha < 1$) also contribute to the interfacial electron transfer.

TABLES.

Table 1. Key morphological parameters of EISA-SnO_2 films determined by ellipsometry.

Template	Withdrawal speed ($mm \cdot s^{-1}$)	Thickness (nm)	Porosity (%)	Pore Size IEP (nm)	Ref
PIB-b-PEO	0.01	250-300	65-70	20-30	This work
PIB-b-PEO	5	80-100	65-70	20-30	This work
KLE	6	110	45,5	7 × 14 §	[21]

§ Ellipsoidal pores

Table of Contents Graphic